ACS APPLIED MATERIALS & INTERFACES

www.acsami.org

Research Article

Bendable and Chemically Stable Metal–Organic Hybrid Membranes for Molecular Separation

Zhigang Wang, Yang Liu, Liyao Wang, Shangwen Zha, Shenxiang Zhang,* and Jian Jin*

Cite This: *ACS Appl. Mater. Interfaces* 2024, 16, 17016–17024

Read Online

ACCESS | Metrics & More | Article Recommendations | Supporting Information

ABSTRACT: Crystalline porous metal–organic materials are ideal building blocks for separation membranes because of their molecular-sized pores and highly ordered pore structure. However, creating ultrathin, defect-free crystalline membranes is challenging due to inevitable grain boundaries. Herein, we reported an amorphous metal–organic hybrid (MOH) membrane with controlled microporosity. The synthesis of the MOH membrane entails the use of titanium alkoxide and organic linkers containing di/multicarboxyl groups as monomers in the polymerization reaction. The resultant membranes exhibit similar microporosity to existing molecular sieve materials and high chemical stability against harsh chemical environments owing to the formation of stable Ti–O bonds between metal centers and organic linkers. An interfacial polymerization is developed to fabricate an ultrathin MOH membrane (thickness of the membrane down to 80 nm), which exhibits excellent rejections (>98% for dyes with molecular weights larger than 690 Da) and high water permeance (55 L m^{-2} h^{-1} bar^{-1}). The membranes also demonstrate good flexibility, which greatly improves the processability of the membrane materials.

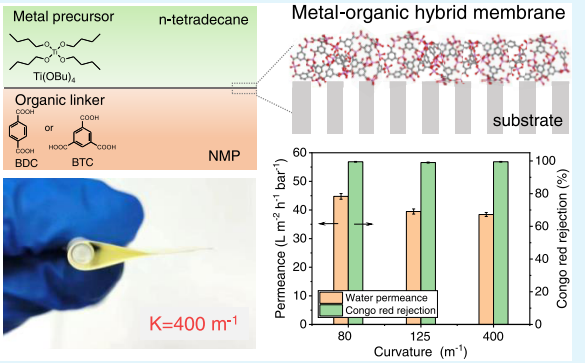

KEYWORDS: *ultrathin membrane, metal–organic hybrid material, microporous material, molecular separation, interfacial polymerization*

1. INTRODUCTION

Membrane-based separation technology has attracted significant attention in the process of purification and separation owing to its high separation efficiency, low operating cost, and process simplicity.[1−4] To further boost membrane separation performance, designing and synthesizing new membrane materials and developing feasible methods to assemble them into defect-free nanofilms with high selectivity and permeance are necessary.[5−8] An ideal membrane should possess high-density molecular-sized pores and a thin selective layer for low-resistance and highly selective permeation.[9−13] Additionally, high chemical stability is required to withstand harsh chemical environments during separation processes.[14−17]

Crystalline porous materials with uniform molecular-sized pores, such as zeolites[18] and metal–organic frameworks (MOFs),[19,20] are promising candidates for high-performance membranes due to their high porosity and uniform pore size distribution.[21,22] In recent years, MOF membranes have gained popularity in membrane material research due to their distinctive structural and chemical versatility compared to zeolites.[23−25] However, MOFs with a polycrystalline nature cannot avoid the existence of grain boundaries or defects in the membrane structure.[26−28] The presence of grain boundaries and defects seriously affects their separation efficiency.[29] Thus, several post-treatment methods, for example, surface coating and chemical vapor deposition modification, have been developed to repair the grain boundary defects and cracks.[30,31] Although the membrane separation performance has improved, the issue of grain boundaries remains unsolved. Very recently, MOF glass membranes were developed, which were fabricated by melt-quenching treatment of a polycrystalline ZIF-62 membrane on a porous support, which was formed via solid–liquid transition followed by the quenching of the corresponding amorphous liquid structure.[32] Although the MOF glass lost its original polycrystalline nature, the porosity remained well and the grain boundary structures were avoided. The molecular sieving ability of the MOF glass membrane was remarkably enhanced. However, there are very few materials that can achieve MOF glass transformation. The MOF glass materials inspire us that direct synthesis of amorphous metal–organic materials is likely to afford the prospective for generating high-performance membranes without grain boundary structures.[33,34]

Received: January 15, 2024
Revised: March 9, 2024
Accepted: March 12, 2024
Published: March 21, 2024

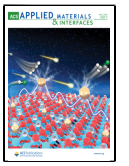

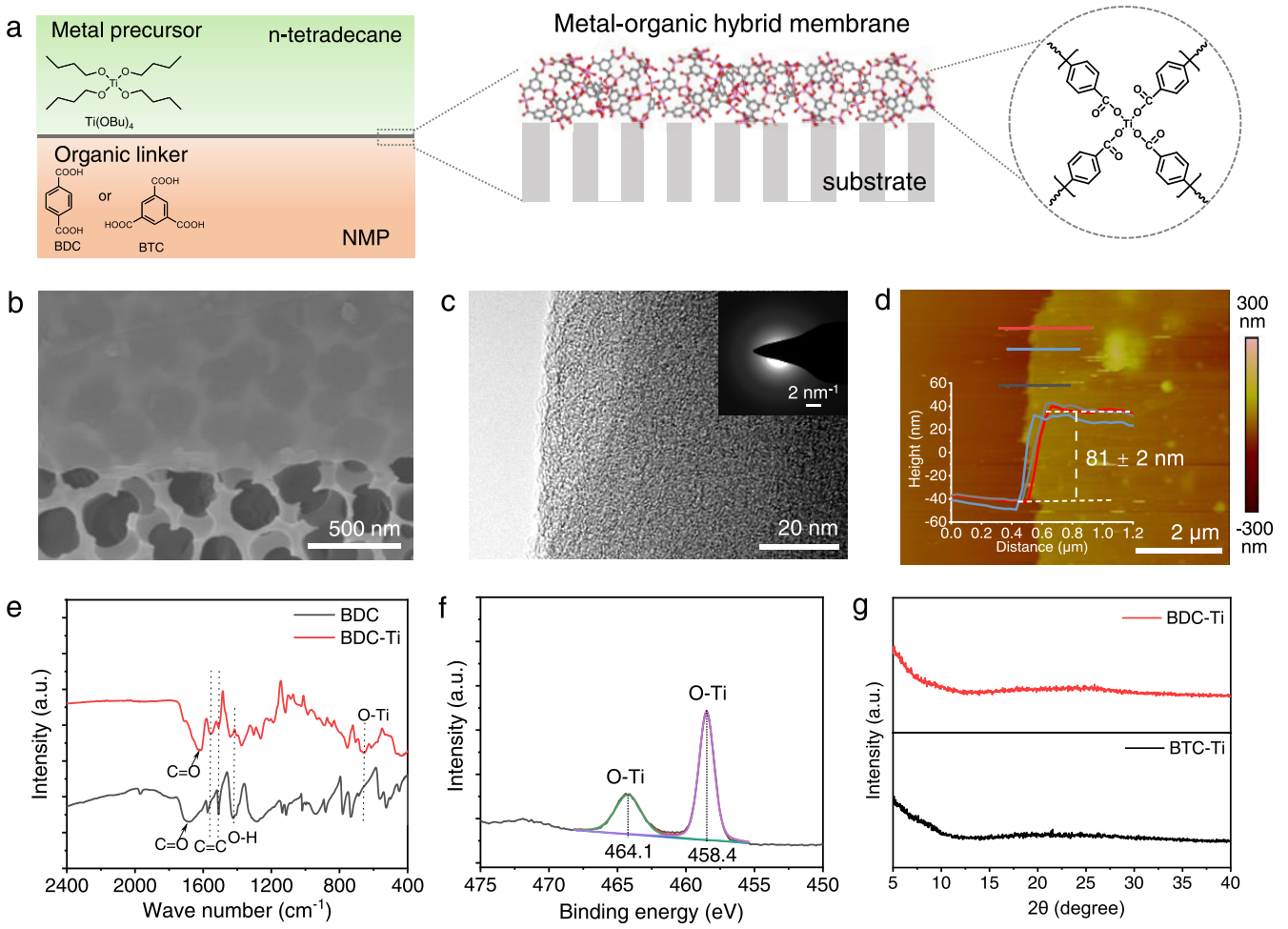

Figure 1. Fabrication and characterization of freestanding MOH membranes. (a) Scheme of interfacial synthesis of MOH membranes. (b) SEM image of BDC-Ti membrane after transferring to an anodized aluminum oxide substrate. (c) TEM image of BDC-Ti membrane. The inset shows a selected area electron diffraction pattern. (d) AFM image and corresponding height profile of the BDC-Ti membrane. (e) FT-IR spectra of the BDC monomer and BDC-Ti membrane. (f) XPS spectrum of BDC-Ti membrane. (g) XRD patterns of BDC-Ti and BTC-Ti membranes.

In this work, we reported an amorphous MOH membrane with controlled microporosity that avoids grain boundary defects while maintaining porous material benefits. The synthesis of an MOH membrane entails the use of titanium alkoxide and organic linkers containing di/multicarboxyl groups as monomers in the interface polymerization reaction. Thanks to the rapid reaction between titanium alkoxide and organic linkers, an ultrathin and defect-free membrane with a thickness of 88 nm can be formed within 30 s through an interfacial polymerization reaction. Although the resultant materials are amorphous, they exhibit microporosity similar to that of existing molecular network materials. The metal−organic hybrid membrane exhibits excellent rejection and high permeance. The membranes also exhibit high chemical stability against harsh chemical environments, such as acid/base solutions and strong polar solvents, owing to the formation of stable Ti−O bonds between metal centers and organic linkers. The MOH membranes also demonstrate good flexibility due to the stable molecular network structure, which greatly improves the processability of membrane materials. Furthermore, MOH membranes could offer a tunable pore size and pore structure via the rational design of organic linkers. This study presents a novel way of producing ultrathin and molecularly selective membranes using interface polymerization.

2. EXPERIMENTAL SECTION

2.1. Materials and Chemicals. 1,4-Benzenedicarboxylic acid (BDC), 1,3,5-benzenetricarboxylic acid, direct red, coomassie bright blue R250, congo red, reactive blue 19, acid fuchsin, crystal violet, methyl orange, and ethane diamine were purchased from Sigma-Aldrich. P84 polyimide was purchased from HP Polymer GmbH. Methanol, ethanol, isopropanol, *n*-butanol, toluene, polyethylene glycol 400 (PEG400), *N*,*N*-dimethylformamide (DMF), *n*-hexane, tetradecane, isooctane, tetrabutyl titanate, and *N*-methyl pyrrolidone (NMP) were obtained from Sinopharm.

2.2. Fabrication of the Polyimide Substrate. The polyimide substrates were fabricated by using a nonsolvent-induced phase separation method. The casting solution was prepared by dissolving 3.8 g of P84 polyimide and 0.8 g of PEG 400 in 17 mL of DMF. After stirring for 12 h, the polymer solution was used to cast films on a clean glass plate at 25 °C and 40% relative humidity. Next, the glass plate was immersed in a water bath at 25 °C. After 4 h, polyimide substrates were transferred to an isopropanol solution and kept for 12 h. After that, the polyimide substrates were immersed in an isopropanol solution containing 200 g/L hexamethylenediamine for 24 h. The membrane was washed with fresh isopropanol to remove any unreacted hexamethylenediamine.

2.3. Preparation of MOH Membranes on the Polyimide Substrate. The supported MOH membranes were synthesized by an

https://doi.org/10.1021/acsami.4c00857
ACS Appl. Mater. Interfaces 2024, 16, 17016−17024

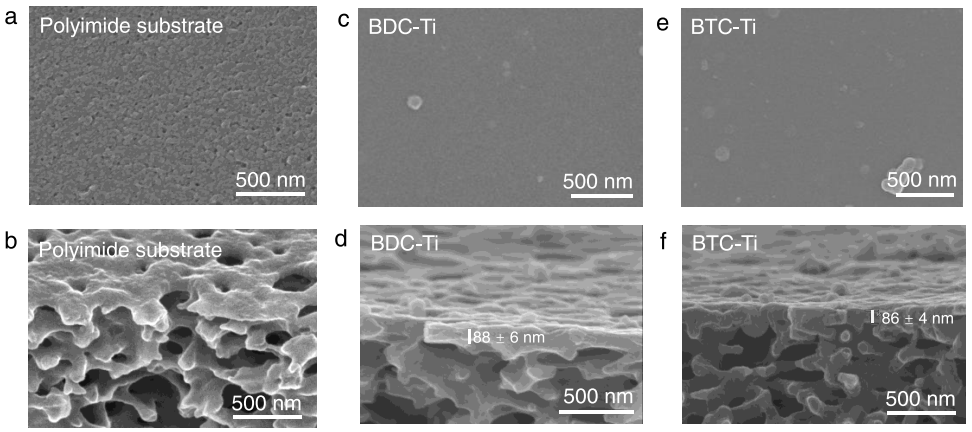

Figure 2. Morphology characterization of MOH membranes supported by the porous polyimide substrate. (a) Surface and (b) cross-sectional SEM images of porous substrate. (c) Surface and (d) cross-sectional SEM images of BDC-Ti membrane prepared by an interfacial reaction of $Ti(OBu)_4$ (2 mM) in tetradecane and BDC (40 mM) in NMP. (e) Surface and (f) cross-sectional SEM images of BTC-Ti membrane prepared by an interfacial reaction of $Ti(OBu)_4$ (2 mM) in tetradecane and BTC (40 mM) in NMP.

interfacial reaction at 25 °C. First, the polyimide support was placed onto a glass plate where 0.5 mL of NMP solution containing organic linkers, BDC or BTC, was preloaded. To make sure that the polyimide support was fully wetted, another 0.5 mL of organic unit solution was dropped onto the surface and allowed to stand for 30 s. Second, the excess solution was removed by dry nitrogen purging until no obvious solution spot could be observed on the surface. Finally, 1.0 mL of tetradecane containing a certain amount of $Ti(OBu)_4$ was then dropped onto the above prewetted membrane surface and stood for 2 min. To remove the excess unreacted precursor solution, the membrane was immersed in hexane and methanol.

2.4. Instruments and Characterizations. Scanning electron microscopy (SEM) images were taken from a Hitachi S8230 scanning electron microscope. Fourier transform infrared (FT-IR) spectra were measured using a Nicolet 6700 Fourier transform infrared spectrometer. The X-ray diffraction (XRD) patterns were obtained using a Bruker D8 instrument equipped with Cu Kα of wavelength λ = 1.54 Å. X-ray photoelectron spectroscopy (XPS, EXCALAB 250 XI) was used to detect the BDC-Ti and BTC-Ti microporous membrane surface properties. The BDC-Ti and BTC-Ti membranes thickness was measured by an atomic force microscope (AFM, Dimension Icon, Bruker). The zeta potential of the MOH membrane was characterized by an electrokinetic analyzer (Sur-PASS 3, Anton Paar, GmbH). The concentration of the dye at the feed and permeate sides was measured by UV−vis spectrophotometry (UV2600i, SHIMADZU). The surface area and pore structure of BDC-Ti and BTC-Ti were determined via a gas adsorption test by using a Quantachrome Autosorb-iQ2 instrument. Before the measurement, samples were evacuated at 120 °C under vacuum (~1×10^{-5} bar) for 12 h.

2.5. Membrane Separation Performance Evaluation. The water flux of BDC-Ti and BTC-Ti membranes was calculated by the following eq 1

$$J = V/(A \times P \times t) \quad (1)$$

In the formula, J (L m^{-2} $h^{-1}$$bar^{-1}$) represents the water flux of BDC-Ti and BTC-Ti membranes, V (L) is the amount of permeated water, t (h) is the testing time, and A (m^2) is the effective membrane area.

The dye rejection, R (%), was calculated using eq 2

$$R = (1 - C_p/C_f) \times 100\% \quad (2)$$

where R (%) is the dye rejection and C_p (ppm) and C_f (ppm) represent the dye concentrations of the permeate and feed solution, respectively.

3. RESULTS AND DISCUSSION

3.1. Fabrication of the MOH Membrane by Interfacial Polymerization. MOH membranes were fabricated through a reaction of organic linkers containing carboxyl groups with tetrabutyl titanate ($Ti(OBu)_4$) at the interface between two immiscible solutions (Figure 1a). Figure S1 shows the self-standing membrane formed at the interface of tetradecane and *N*-methyl pyrrolidone (NMP). The resulting MOH membranes were denoted as BDC-Ti and BTC-Ti, respectively, reflecting the use of 1,4-benzenedicarboxylic acid (BDC) and 1,3,5-benzenetricarboxylic acid (BTC) as organic linkers. The interfacial polymerization reaction entailed a transesterification reaction between metal alkoxides and carboxyl groups within the organic linkers, as depicted in the reaction scheme in Figure S2.

Figure 1b shows the scanning electron microscopy (SEM) image of a BDC-Ti membrane transferred onto an anodized aluminum (AAO) substrate. The surface of the BDC-Ti membrane was smooth and no obvious pinholes or cracks were observed. The transmission electron microscopy (TEM) image and selected area electron diffraction pattern in Figure 2c demonstrate the amorphous nature of the BDC-Ti membrane. The thickness of the BDC-Ti membrane was determined by using atomic force microscopy (AFM) after being transferred onto a silicon wafer (Figure 1d). The measured thickness was 81 ± 2 nm. Freestanding BTC-Ti membranes were also obtained following the same interfacial synthesis method (Figures S3 and S4).

The chemical compositions of MOH membranes were investigated through Fourier transform infrared spectroscopy (FT-IR) and X-ray photoelectron spectroscopy (XPS). FT-IR spectra displayed adsorption peaks at 1573 and 1452 cm^{-1} corresponding to the vibrational modes of the C═C bonds in the benzene rings (Figure 2e). In BDC-Ti samples, O−H vibrational peaks at 1420 cm^{-1} disappeared, and a new peak appeared at 660 cm^{-1} corresponding to the O−Ti bond, indicating a high conversion of O−H to O−Ti. Notably, the presence of neighboring Ti^{4+} ions induced changes in the charge distribution within the functional group, subsequently altering the bond force constant. This alteration resulted in a blue shift in the absorption peak of C═O, shifting to 1600 cm^{-1} when compared to that of the ligand BDC. The same results can be observed in the BTC-Ti sample (Figure S5).

https://doi.org/10.1021/acsami.4c00857
ACS Appl. Mater. Interfaces 2024, 16, 17016−17024

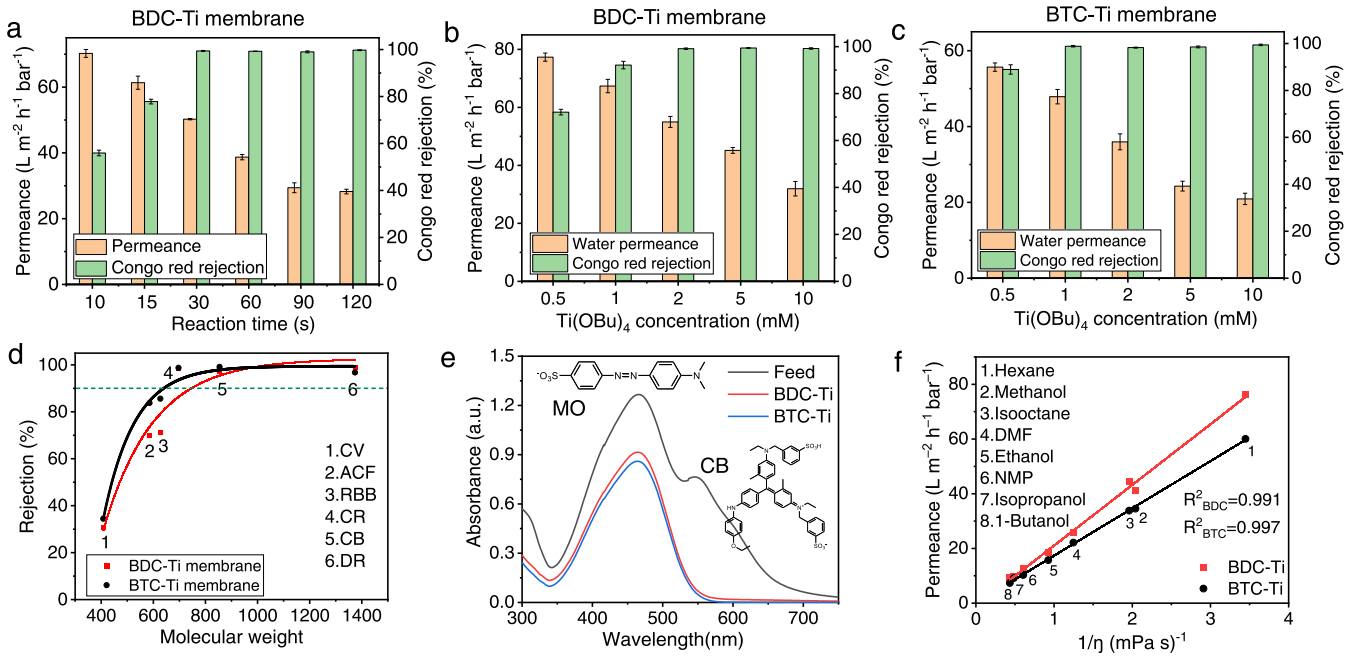

Figure 3. Separation performance of MOH membranes. (a) Water performance and CR rejection of BDC-Ti membranes with different reaction times. The effect of $Ti(OBu)_4$ concentration on the separation performance of (b) BDC-Ti and (c) BTC-Ti membranes. In this experiment, the concentration of BDC or BTC was kept at 40 mM and the concentration of $Ti(OBu)_4$ was adjusted in the range of 0.5−10 mM. Water permeance and CR rejection were recorded. (d) Rejection of selected dyes in water versus their molecular weight. (e) UV−vis absorbance spectra of a mixture solution of CB and MO before and after filtration through the BDC-Ti or BTC-Ti membrane. (f) Permeance of pure organic solvents through BDC-Ti or BTC-Ti membrane.

Furthermore, the survey XPS spectra of BDC-Ti and BTC-Ti membranes show the major peaks of carbon, oxygen, and titanium elements (Figure S6), the high-resolution XPS spectra of titanium (Figure 1d) present two distinct energy bands at 458.4 and 464.1 eV, which are typical values of Ti $2p_{2/3}$ and Ti $2p_{1/3}$ electrons for Ti^{4+}, respectively, confirming the presence of the metal ions in the molecular network membrane in their quadrivalent states.

Figure 1e shows the X-ray diffraction (XRD) patterns of BDC-Ti and BTC-Ti membranes. There are no obvious diffraction peaks, suggesting that the resulting MOH membranes possessed an amorphous structure, consistent with the results obtained from selected area electron diffraction (SAED). The possible reason is that the reaction between $Ti(OBu)_4$ and organic linkers is too fast, leaving insufficient time for nucleation and growth processes.[34,35] The porous structure of MOH materials was characterized by N_2 adsorption at 77 K. As shown in Figure S7a, both BDC-Ti and BTC-Ti materials exhibited a sharp increase at low relative pressure (P/P_0 < 0.05), indicating a microporous structure. The N_2 adsorption amount continued to increase at a higher relative pressure, suggesting multilayer adsorption and the existence of mesopores. We also conducted CO_2 adsorption isothermal tests for BDC-Ti and BTC-Ti powder at 273 K (Figure S7b) because CO_2 has a smaller kinetic diameter (3.3 Å) than that of N_2 (3.6 Å), allowing it to access micropores that are inaccessible to N_2. The CO_2 adsorption isotherms at 273 K revealed Brunauer−Emmett−Teller (BET) surface areas of 41.7 $m^2\ g^{-1}$ for BDC-Ti and 34.4 $m^2\ g^{-1}$ for BTC-Ti. In particular, BDC-Ti exhibited a predominant pore size distribution ranging from 4 to 6 Å, while BTC-Ti displayed pores primarily distributed in the range of 3−4.5 Å (Figure S7c). This suggested that the organic linkers can be used to tune the pore size of MOH membranes. Additionally, the surface charge characteristics of the membranes were explored via surface ζ-potential measurements, which indicated isoelectric points of pH 4.6 for BDC-Ti and pH 5.7 for BTC-Ti (Figure S8). In the pH range between 6.0 and 9.0, the surface zeta potential exhibited slight negativity with values below −10 mV.

To avoid damage to the membrane during the transfer process, we also directly fabricated MOH membranes on a cross-linked polyimide substrate. On the surface of the polyimide substrate, numerous small pores are evenly distributed (Figure 2a,b). After the interface reaction of BDC and $Ti(OBu)_4$ on the surface of the polyimide substrate, a continuous, defect-free selective layer was formed on the support layer (Figure 2c,d). The thickness of the BDC-Ti membrane is about 88 nm, which is in accordance with the result measured by AFM. Using the same method, after the interfacial reaction of BTC and $Ti(OBu)_4$ on the surface of a polyimide substrate, a continuous BTC-Ti membrane can be formed, with a thickness of 86 nm (Figure 2e,f).

3.2. Separation Performance of MOH Membranes. To achieve an optimal condition, we studied the influence of interfacial reaction time and tetrabutyl titanate concentration on the BDC-Ti membrane's performance. As the reaction time increased, the surface of BDC-Ti membranes transformed from porous to dense and defect-free (Figure S9). As presented in Figure 3a, for the BDC-Ti membrane with 10 s reaction time, water permeance was as high as 70.3 L $m^{-2}\ h^{-1}\ bar^{-1}$, but the rejection rate for congo red (CR, molecular weight of 696.7 g mol^{-1}) was only 56.0%. This indicated a less compact structure with larger average pore size than the CR molecule in such a thin membrane. When the BDC-Ti membrane reaction time increased to 30 s, water permeance decreased to 50.3 L m^{-2}

https://doi.org/10.1021/acsami.4c00857
ACS Appl. Mater. Interfaces 2024, 16, 17016−17024

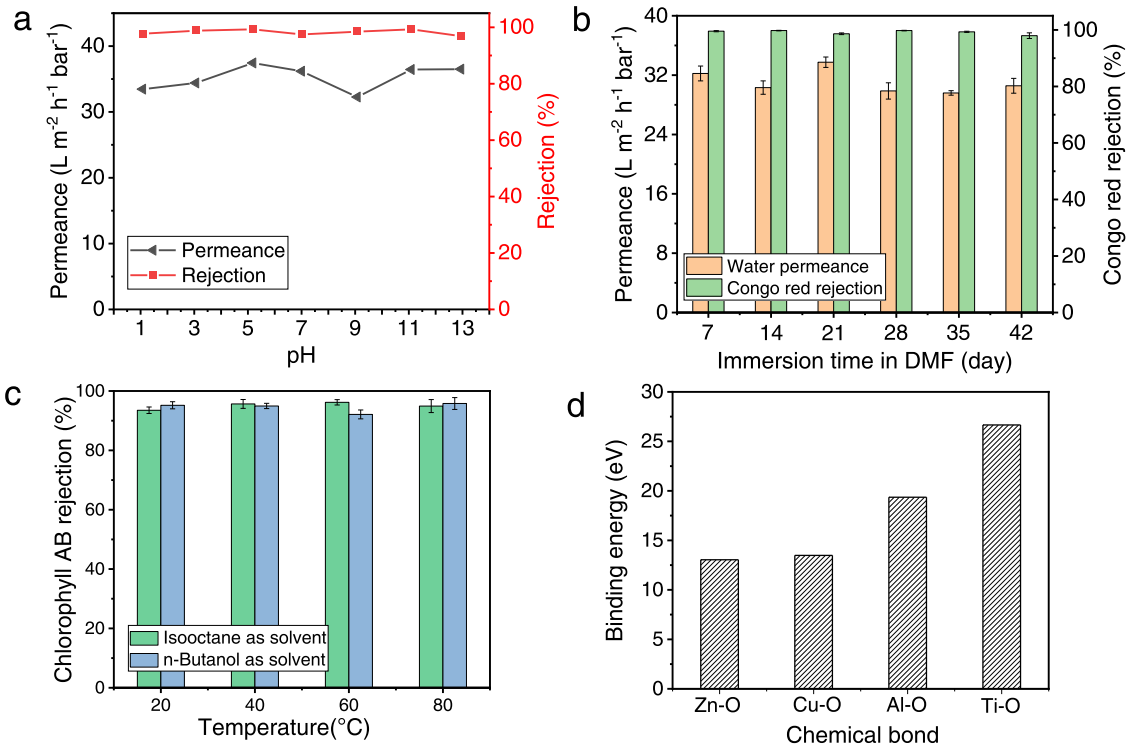

Figure 4. Chemical stability test. (a) Water permeance and CB rejection of the BDC-Ti membrane at different pH values. (b) Water permeance and CR rejection of the BDC-Ti membrane after soaking in DMF for a certain time. (c) Chlorophyll AB rejection of the BDC-Ti membrane at elevated temperatures with isooctane or *n*-butanol as the solvent. (d) Comparison of Ti−O bonding energy with other metal−oxide bonds, such as Zn−O, Cu−O, and Al−O.

h^{-1} bar^{-1}, and rejection for CR increased to 99.4%, suggesting significantly narrowed membrane pores that were smaller than the CR molecule. With a further increases in reaction time to 90 and 120 s, water permeance exhibited only a slight decrease, reaching 29.4 and 28.2 L m^{-2} h^{-1} bar^{-1}, with CR rejection rates increasing to 99.0 and 99.7%, respectively. These results indicate that with increasing reaction time, rejection gradually improves, while permeability moderately declines. Apparently, with 30 s reaction time, the CR permeability reached 31.1 L m^{-2} h^{-1} bar^{-1}, with a rejection of 99.4%, indicating an optimal balance between rejection and permeability.

Next, we studied the effect of $Ti(OBu)_4$ concentrations during the fabrication of BDC-Ti and BTC-Ti membranes on separation performance. Specifically, we adjusted $Ti(OBu)_4$ concentrations ranging from 0.5 to 10 mM. When the $Ti(OBu)_4$ concentrations were lower than 2 mM, the obtained BDC-Ti membrane surface exhibited a porous structure (Figure S10), indicating that it is hard to form a continuous structure. As the $Ti(OBu)_4$ concentration increased to 2 mM, organic molecules and $Ti(OBu)_4$ increasingly clumped together to form a more compact structure until a dense and defect-free selective layer was established. We evaluated the separation performance of these BDC-Ti membranes using 50 ppm CR aqueous solution. Figure 3b reveals that as the $Ti(OBu)_4$ concentration increased from 0.5 to 10 mM, the CR rejection rate for the resulting BDC-Ti membranes increased from 72.1 to 99.2% (Figure S11). Simultaneously, water permeance decreased from 77.3 to 31.9 L m^{-2} h^{-1} bar^{-1}, indicating the formation of a denser membrane at higher $Ti(OBu)_4$ concentrations during the interfacial reaction process. Similar results were observed in the BTC-Ti membranes (Figure 3c). Comparative analysis demonstrated that when the BDC/BTC concentration was 40 mM and the tetrabutyl titanate concentration was 2 mM, it ensured both high rejection and good permeability. Specifically, the rejection of BDC-Ti and BTC-Ti for CR reached 99.1 and 98.3%, respectively, while the permeability measured 55.0 and 36.0 L m^{-2} h^{-1} bar^{-1}, respectively. Subsequent experiments and tests were conducted at a concentration of 2 mM $Ti(OBu)_4$ and 40 mM BDC or BTC.

Under the optimal conditions, we subjected dyes of varying molecular sizes to testing, including direct red (DR, molecular weight 1373.1 g mol^{-1}), coomassie bright blue R250 (CB, 826.0 g mol^{-1}), congo red (CR, 696.7 g mol^{-1}), reactive blue 19 (RBB, 626.5 g mol^{-1}), acid fuchsin (ACF, 585.5 g mol^{-1}), and crystal violet (CV, 408.0 g mol^{-1}) (the molecular structures of the dyes are presented in Table S1). Figure 3d shows dye rejection as a function of MW. The BDC-Ti membrane showed low rejection for CV and ACF, measured at 30.8 and 69.9%, respectively (Figure S12). For dyes with larger molecular structures such as CR, CB, and DR, their rejection increased to 98.3, 97.5, and 98.9%, respectively. These findings suggested that the BDC-Ti membrane exhibits a molecular weight cutoff (MWCO) of 690 Da. In the case of the BTC-Ti membrane, rejection for CV and ACF was 37.4 and 83.9%, respectively, but for CR, CB, and DR, their rejection was notably higher, measuring at 98.8, 99.2, and 96.8%, respectively. Based on the results obtained, it can be calculated that the MWCO of BTC-Ti is 640 Da, which is smaller than that of BDC-Ti, consistent with the pore size distribution data obtained from the above CO_2 isotherm adsorption tests. To verify the molecular sieving capability of the MOH membranes, the separation of a mixed solution of MO (327.3 g mol^{-1}) and CB was carried out. Figure 3e shows

https://doi.org/10.1021/acsami.4c00857
ACS Appl. Mater. Interfaces 2024, 16, 17016−17024

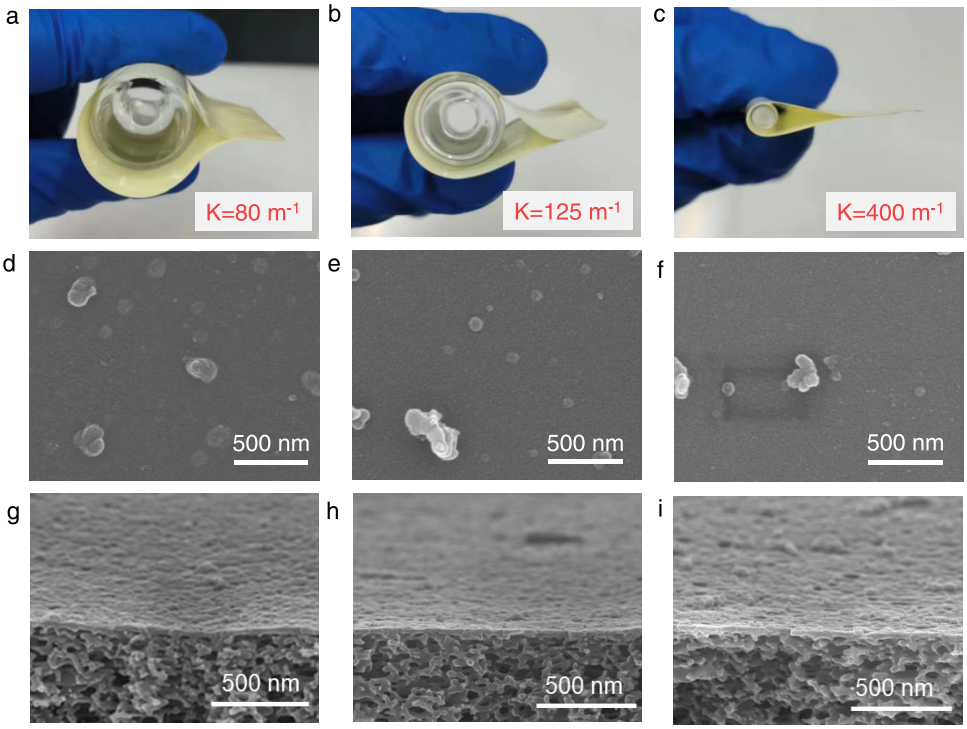

Figure 5. (a–c) Photographs of the bending BDC-Ti membranes with different curvatures. The curvature K of the bend is the reciprocal of the radius ($K = 1/r$). (d–f) Surface and (g–i) cross-sectional SEM images of the BDC-Ti membrane after bending with different curvatures. (a, d, g) $K = 80\ m^{-1}$; (b, e, h) $K = 125\ m^{-1}$; and (c, f, i) $K = 400\ m^{-1}$.

the UV–vis spectra of the feed and the permeate after filtration. Clearly, after filtration, almost no CB molecules passed through the membrane, and the CB rejections of BDC-Ti and BTC-Ti membranes are above 98.0%. As for MO, BDC-Ti and BTC-Ti membranes presented a low rejection rate of 28.4 and 32.5%, respectively. This result demonstrates a sharp separation between two dyes with different molecular structures by using MOH membranes.

Permeance of organic solvents, including polar and nonpolar solvents (e.g., methanol, ethanol, isopropanol, *n*-butanol, DMF, NMP, isooctane, and *n*-hexane), through BDC-Ti and BTC-Ti membranes was measured. Figure 3f demonstrates that the permeance of the solvents increased inversely with their viscosity. For membranes with a microporous structure, viscous flow can be readily explained by the Hagen–Poiseuille equation.[36] Generally, the BDC-Ti membrane exhibited higher organic solvent permeance than that of the BTC-Ti membrane, probably because of its larger pore size.

3.3. Stability Test of the MOH Membranes. Stability is an essential parameter for the MOH membrane, considering separation in harsh chemical environments. To evaluate the chemical stability of MOH membranes, they were exposed to different chemical environments, including strong acid/base solutions and polar organic solvents. To evaluate the stability of the BDC-Ti membrane, we adjusted the pH value of CB solutions within the range of 1 to 14. In Figure 4a, it can be seen that the BDC-Ti membrane has high CB rejection rates above 97% when the pH is in the range of 1–13. However, the BDC-Ti membrane exhibited a rejection rate of only 60.8% for the CB solution when at a pH of 14. Additionally, the water permeance remains around 35 L m^{-2} h^{-1} bar^{-1} within the pH range of 1–13. The BTC-Ti membrane also presented stable separation performance in a broad pH range (Figure S13), indicating that the MOH membranes have outstanding pH stability. For effective separation, MOH membrane pores should be rigid in harsh solvents and at elevated temperatures. We observed that after soaking the MOH membranes in DMF for 42 days, they maintained the initial water permeance and CR rejection (Figures 4b and S14). Additionally, the BDC-Ti membrane's thermal stability was tested at elevated temperatures using different solvents. The rejection of chlorophyll AB was monitored as an indicator of stability. Figure S15 shows the setup for the thermal stability test at elevated temperatures. At 20 °C, the rejection for chlorophyll AB in isooctane and *n*-butanol was measured to be 93.5 and 95.2%, respectively. Notably, even under the elevated temperature of 80 °C, the rejection remained impressively high, reaching 94.9% in isooctane and 95.8% in *n*-butanol (Figures 4c and S16). These results indicated that the MOH membranes maintain exceptional stability and rejection, even at elevated temperatures.

To elucidate the reason why the MOH membranes had such excellent stability, metal–oxygen bonding energy between the metal center and organic linker was calculated based on density functional theory (DFT; for detailed information, see Table S2). Besides the Ti–O bond, Zn–O, Cu–O, and Al–O bonds were also calculated as a comparison. As illustrated in Figure 4d, the bonding energy values for Ti–O, Al–O, Cu–O, and Zn–O are approximately 26.7, 19.4, 13.5, and 13.0 eV, respectively. Notably, O–Ti exhibits the highest bonding energy, possibly owing to the smaller ionic radius of high-valent metals compared with low-valent metals, resulting in heightened reactivity and oxygen affinity in high-valent metals. The higher valence states of metal ions increase their polarization ability.[37−39] This improves the bonding energy between the metal and ligand, enhancing membrane stability.

The mechanical properties of the membrane are also crucial for practical applications. A series of toughness tests with

https://doi.org/10.1021/acsami.4c00857
ACS Appl. Mater. Interfaces 2024, 16, 17016−17024

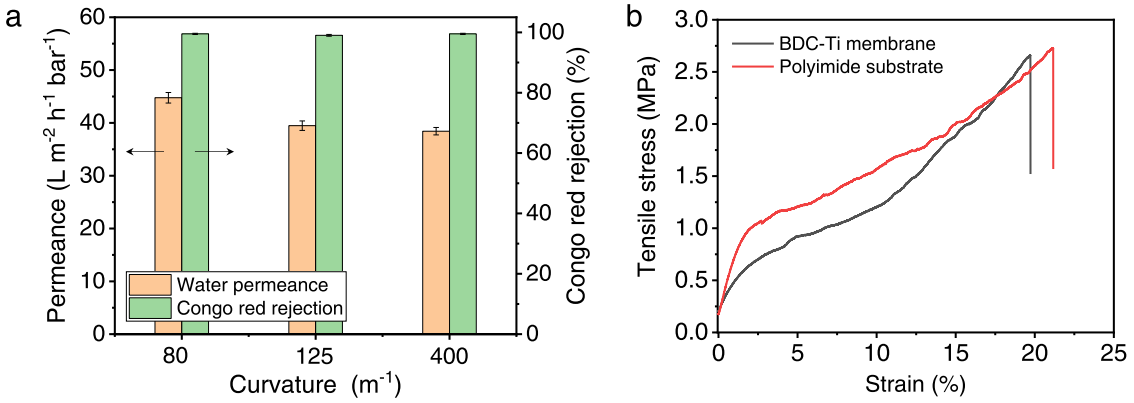

Figure 6. (a) Separation performance of BDC-Ti membranes after bending with different curvatures. (b) Stress−strain curves of polyimide substrate and BDC-Ti membrane.

different bending degrees of the polyimide-supported BDC-Ti membranes are explored (Figure 5a−c). According to the SEM images of the BDC-Ti membranes, there were no visible cracks, fragmentation, or detachment of the membrane layer observed after bending, with curvatures ranging from 80 to 400 m^{-1} (as shown in Figure 5d−i). This study indicates that the BDC-Ti membrane retains its flexibility under both tensile and compressive stress. More importantly, the rejection of the BDC-Ti membrane after bending with a curvature of 80 m^{-1} remains at 99.5%, while the permeability remains at 44.8 L m^{-2} h^{-1} bar^{-1}, which is the same as the initial performance before bending (as shown in Figures 6a and S17). This exceptional stability continues even when the curvature reaches 400 m^{-1}. The stress−strain curves of the polyimide substrate and BDC-Ti membrane were measured to evaluate their mechanical properties. As shown in Figure 6b, the polyimide substrate had a tensile strength of 2.72 MPa and an elongation of 21.07%. After forming an 88 nm-thick BDC-Ti membrane on the surface of the polyimide substrate, the tensile strength decreased to 2.65 MPa, while the elongation slightly reduced to 19.68%. These results suggest that the BDC-Ti membrane retained the original mechanical properties and flexibility of the polyimide substrate.

4. CONCLUSIONS

In summary, we proposed an interface polymerization strategy for the fabrication of ultrathin films with controlled microporosity. The strategy involves using titanium alkoxide and organic linkers that contain di/multicarboxyl groups as monomers in the reaction. An ultrathin and defect-free membrane with a thickness of ∼80 nm can be formed within 30 s through an interfacial polymerization reaction. Although the resulting MOH materials are amorphous, they exhibit a good membrane-forming property and excellent separation performance. Owing to the stable Ti−O bond formed between metal centers and organic linkers, the MOH membranes present high chemical stability against harsh chemical environments, such as acid/base solutions and strong polar solvents. The MOH membranes also demonstrate good flexibility due to their molecular network structure, which greatly improves the processability of membrane materials. This work presents a new approach to creating ultrathin MOH membranes through interface polymerization.

ASSOCIATED CONTENT

Supporting Information

The Supporting Information is available free of charge at https://pubs.acs.org/doi/10.1021/acsami.4c00857.

Additional SEM, FT-IR, and XPS characterizations, CO_2 adsorption isotherm at 273 K for BDC-Ti and BTC-Ti powders, surface streaming potential of BDC-Ti and BTC-Ti membranes, UV−vis spectra of the feed solution and permeate solutions after filtering through MOH membranes, and calculation of bond energy (PDF)

AUTHOR INFORMATION

Corresponding Authors

Shenxiang Zhang − *College of Chemistry, Chemical Engineering and Materials Science, Soochow University, Suzhou 215123 Jiangsu, China; Jiangsu Key Laboratory of Advanced Functional Polymer Design and Application, Jiangsu Key Laboratory of Advanced Negative Carbon Technologies, Soochow University, Suzhou 215123 Jiangsu, China;* orcid.org/0000-0003-2857-333X; Email: sxzhang@suda.edu.cn

Jian Jin − *College of Chemistry, Chemical Engineering and Materials Science, Soochow University, Suzhou 215123 Jiangsu, China; Jiangsu Key Laboratory of Advanced Functional Polymer Design and Application, Jiangsu Key Laboratory of Advanced Negative Carbon Technologies, Soochow University, Suzhou 215123 Jiangsu, China;* orcid.org/0000-0003-0429-300X; Email: jjin@suda.edu.cn

Authors

Zhigang Wang − *College of Chemistry, Chemical Engineering and Materials Science, Soochow University, Suzhou 215123 Jiangsu, China*

Yang Liu − *College of Chemistry, Chemical Engineering and Materials Science, Soochow University, Suzhou 215123 Jiangsu, China; Jiangsu Key Laboratory of Advanced Functional Polymer Design and Application, Jiangsu Key Laboratory of Advanced Negative Carbon Technologies, Soochow University, Suzhou 215123 Jiangsu, China;* orcid.org/0000-0002-1789-6937

Liyao Wang − *College of Chemistry, Chemical Engineering and Materials Science, Soochow University, Suzhou 215123 Jiangsu, China*

Shangwen Zha − *College of Chemistry, Chemical Engineering and Materials Science, Soochow University, Suzhou 215123 Jiangsu, China; Department of Research and Development, Shanghai ECO Polymer Sci.&Tech. CO., Ltd, Shanghai 201306, China*

Complete contact information is available at: https://pubs.acs.org/10.1021/acsami.4c00857

Author Contributions

S.Zhang and J.J. designed the project. Z.W., Y.L., and L.W. synthesized and characterized the membranes and evaluated the separation performance. S.Zha provided suggestions and technical support. Z.W., S.Zhang, Y.L., and J.J. wrote and edited the article. J.Jin supervised the project.

Notes

The authors declare no competing financial interest.

■ ACKNOWLEDGMENTS

This work was supported by the National Key Research and Development Program of China (2022YFB3805903), the National Natural Science Foundation of China (22208229, 21988102), the Key Research and Development Plan of Jiangsu Province (BE2022056), the Natural Science Foundation of Jiangsu Province (BK20220501), and the Gusu Innovation and Entrepreneurship Leading Talent Plan (ZXL2023198). Y. Liu thanks the China Postdoctoral Science Foundation (2023M732522) and the Jiangsu Excellent Postdoctoral Project (2023ZB206) for financial support.

■ REFERENCES

(1) Liang, B.; Wang, H.; Shi, X.; Shen, B.; He, X.; Ghazi, Z. A.; Khan, N. A.; Sin, H.; Khattak, A. M.; Li, L.; Tang, Z. Microporous Membranes Comprising Conjugated Polymers with Rigid Backbones Enable Ultrafast Organic-Solvent Nanofiltration. *Nat. Chem.* **2018**, *10* (9), 961−967.

(2) Zhang, G.; Li, X.; Chen, G.; Zhang, Y.; Wei, M.; Chen, X.; Li, B.; Wu, Y.; Wu, L. Supramolecular Framework Membrane for Precise Sieving of Small Molecules, Nanoparticles and Proteins. *Nat. Commun.* **2023**, *14* (1), No. 975, DOI: 10.1038/s41467-023-36684-w.

(3) Dou, H.; Xu, M.; Wang, B.; Zhang, Z.; Wen, G.; Zheng, Y.; Luo, D.; Zhao, L.; Yu, A.; Zhang, L.; Jiang, Z.; Chen, Z. Microporous Framework Membranes for Precise Molecule/Ion Separations. *Chem. Soc. Rev.* **2021**, *50* (2), 986−1029.

(4) Fan, H.; Wang, H.; Peng, M.; Meng, H.; Mundstock, A.; Knebel, A.; Caro, J. Pore-in-Pore Engineering in a Covalent Organic Framework Membrane for Gas Separation. *ACS Nano* **2023**, *17* (8), 7584.

(5) Jimenez-Solomon, M. F.; Song, Q.; Jelfs, K. E.; Munoz-Ibanez, M.; Livingston, A. G. Polymer nanofilms with enhanced microporosity by interfacial polymerization. *Nat. Mater.* **2016**, *15* (7), 760−767.

(6) Yang, Q.; Su, Y.; Chi, C.; Cherian, C. T.; Huang, K.; Kravets, V. G.; Wang, F. C.; Zhang, J. C.; Pratt, A.; Grigorenko, A. N.; Guinea, F.; Geim, A. K.; Nair, R. R. Ultrathin Graphene-Based Membrane with Precise Molecular Sieving and Ultrafast Solvent Permeation. *Nat. Mater.* **2017**, *16* (12), 1198−1202.

(7) Chen, L.; Shi, G.; Shen, J.; Peng, B.; Zhang, B.; Wang, Y.; Bian, F.; Wang, J.; Li, D.; Qian, Z.; Xu, G.; Liu, G.; Zeng, J.; Zhang, L.; Yang, Y.; Zhou, G.; Wu, M.; Jin, W.; Li, J.; Fang, H. Ion Sieving in Graphene Oxide Membranes via Cationic Control of Interlayer Spacing. *Nature* **2017**, *550* (7676), 380−383.

(8) Park, H. B.; Kamcev, J.; Robeson, L. M.; Elimelech, M.; Freeman, B. D. Maximizing the Right Stuff: The Trade-off between Membrane Permeability and Selectivity. *Science* **2017**, *356* (6343), 1138−1148, DOI: 10.1126/science.aab0530.

(9) Zhang, P.; Chen, S.; Zhu, C.; Hou, L.; Xian, W.; Zuo, X.; Zhang, Q.; Zhang, L.; Ma, S.; Sun, Q. Covalent Organic Framework Nanofluidic Membrane as a Platform for Highly Sensitive Bionic Thermosensation. *Nat. Commun.* **2021**, *12*, No. 1844, DOI: 10.1038/s41467-021-22141-z.

(10) Jiang, C.; Zhang, L.; Li, P.; Sun, H.; Hou, Y.; Niu, Q. J. Ultrathin Film Composite Membranes Fabricated by Novel In Situ Free Interfacial Polymerization for Desalination. *ACS Appl. Mater. Interfaces* **2020**, *12* (22), 25304−25315.

(11) Dong, Y.; Cheng, Y.; Xu, G.; Cheng, H.; Huang, K.; Duan, J.; Mo, D.; Zeng, J.; Bai, J.; Sun, Y.; Liu, J.; Yao, H. Selectively Enhanced Ion Transport in Graphene Oxide Membrane/PET Conical Nanopore System. *ACS Appl. Mater. Interfaces* **2019**, *11* (16), 14960−14969.

(12) Wang, Z.; Wang, Z.; Lin, S.; Jin, H.; Gao, S.; Zhu, Y.; Jin, J. Nanoparticle-Templated Nanofiltration Membranes for Ultrahigh Performance Desalination. *Nat. Commun.* **2018**, *9* (1), No. 2004, DOI: 10.1038/s41467-018-04467-3.

(13) Zhao, G. J.; Li, L. L.; Gao, H. Q.; Zhao, Z. J.; Pang, Z. F.; Pei, C. L.; Qu, Z.; Dong, L. L.; Rao, D. W.; Caro, J.; Meng, H. Polyamide Nanofilms through a Non-Isothermal-Controlled Interfacial Polymerization. *Adv. Funct. Mater.* **2024**, No. 2313026, DOI: 10.1002/adfm.202313026.

(14) Tang, C. Y.; Yang, Z.; Guo, H.; Wen, J. J.; Nghiem, L. D.; Cornelissen, E. Potable Water Reuse through Advanced Membrane Technology. *Environ. Sci. Technol.* **2018**, *52* (18), 10215−10223.

(15) Xia, Z.; Song, Y. F.; Shi, S. Interfacial Preparation of Polyoxometalate-Based Hybrid Supramolecular Polymers by Orthogonal Self-Assembly. *Angew. Chem., Int. Ed.* **2024**, *63* (6), No. e202312187, DOI: 10.1002/anie.202312187.

(16) Huang, T.; Moosa, B. A.; Hoang, P.; Liu, J.; Chisca, S.; Zhang, G.; AlYami, M.; Khashab, N. M.; Nunes, S. P. Molecularly-Porous Ultrathin Membranes for Highly Selective Organic Solvent Nanofiltration. *Nat. Commun.* **2020**, *11* (1), No. 5882, DOI: 10.1038/s41467-020-19404-6.

(17) Ding, J.; Wu, H.; Wu, P. Multirole Regulations of Interfacial Polymerization Using Poly(acrylic acid) for Nanofiltration Membrane Development. *ACS Appl. Mater. Interfaces* **2021**, *13* (44), 53120−53130.

(18) Rangnekar, N.; Mittal, N.; Elyassi, B.; Caro, J.; Tsapatsis, M. Zeolite Membranes - a Review and Comparison with MOFs. *Chem. Soc. Rev.* **2015**, *44* (20), 7128−7154.

(19) Qian, Q.; Asinger, P. A.; Lee, M. J.; Han, G.; Mizrahi Rodriguez, K.; Lin, S.; Benedetti, F. M.; Wu, A. X.; Chi, W. S.; Smith, Z. P. MOF-Based Membranes for Gas Separations. *Chem. Rev.* **2020**, *120* (16), 8161−8266.

(20) Denny, M. S.; Moreton, J. C.; Benz, L.; Cohen, S. M. Metal−Organic Frameworks for Membrane-Based Separations. *Nat. Rev. Mater.* **2016**, *1* (12), No. 16078, DOI: 10.1038/natrevmats.2016.78.

(21) Qiao, Z.; Zhao, S.; Sheng, M.; Wang, J.; Wang, S.; Wang, Z.; Zhong, C.; Guiver, M. D. Metal-Induced Ordered Microporous Polymers for Fabricating Large-Area Gas Separation Membranes. *Nat. Mater.* **2019**, *18* (2), 163−168.

(22) Knebel, A.; Bavykina, A.; Datta, S. J.; Sundermann, L.; Garzon-Tovar, L.; Lebedev, Y.; Durini, S.; Ahmad, R.; Kozlov, S. M.; Shterk, G.; Karunakaran, M.; Carja, I. D.; Simic, D.; Weilert, I.; Klüppel, M.; Giese, U.; Cavallo, L.; Rueping, M.; Eddaoudi, M.; Caro, J.; Gascon, J. Solution Processable Metal-Organic Frameworks for Mixed Matrix Membranes Using Porous Liquids. *Nat. Mater.* **2020**, *19* (12), 1346−1353.

(23) Guan, X.; Li, H.; Ma, Y.; Xue, M.; Fang, Q.; Yan, Y.; Valtchev, V.; Qiu, S. Chemically Stable Polyarylether-Based Covalent Organic Frameworks. *Nat. Chem.* **2019**, *11* (6), 587−594.

(24) Cai, G.; Yan, P.; Zhang, L.; Zhou, H. C.; Jiang, H. L. Metal-Organic Framework-Based Hierarchically Porous Materials: Synthesis and Applications. *Chem. Rev.* **2021**, *121* (20), 12278−12326.

(25) Cong, S.; Yuan, Y.; Wang, J.; Wang, Z.; Kapteijn, F.; Liu, X. Highly Water-Permeable Metal−Organic Framework MOF-303 Membranes for Desalination. *J. Am. Chem. Soc.* **2021**, *143* (48), 20055−20058.
(26) Fonseca, J.; Gong, T.; Jiao, L.; Jiang, H.-L. Metal−Organic Frameworks (MOFs) Beyond Crystallinity: Amorphous MOFs, MOF Liquids and MOF Glasses. *J. Mater. Chem. A* **2021**, *9* (17), 10562−10611.
(27) Liu, X.; Demir, N. K.; Wu, Z.; Li, K. Highly Water-Stable Zirconium Metal−Organic Framework UiO-66 Membranes Supported on Alumina Hollow Fibers for Desalination. *J. Am. Chem. Soc.* **2015**, *137* (22), 6999−7002.
(28) Zhang, S.; Ciora, R.; Sengupta, B.; Li, H.; Belfort, G.; Li, S.; Zhou, R.; Yu, M. Ultrathin microporous metal−organic network membranes for molecular separation. *J. Mater. Chem. A* **2021**, *9* (45), 25531−25538.
(29) Lin, R.; Hou, J.; Li, M.; Wang, Z.; Ge, L.; Li, S.; Smart, S.; Zhu, Z.; Bennett, T. D.; Chen, V. Interfacial Engineering of a Polymer−MOF Composite by in Situ Vitrification. *Chem. Commun.* **2020**, *56* (25), 3609−3612.
(30) Liu, Y.; Wei, Y.; Liu, M.; Bai, Y.; Wang, X.; Shang, S.; Chen, J.; Liu, Y. Electrochemical Synthesis of Large Area Two-Dimensional Metal−Organic Framework Films on Copper Anodes. *Angew. Chem., Int. Ed.* **2021**, *60* (6), 2887−2891.
(31) Li, S. L.; Chang, G. L.; Huang, Y. Z.; Kinooka, K.; Chen, Y. T.; Fu, W. M.; Gong, G. H.; Yoshioka, T.; McKeown, N. B.; Hu, Y. X. 2,2′-Biphenol-Based Ultrathin Microporous Nanofilms for Highly Efficient Molecular Sieving Separation. *Angew. Chem., Int. Ed.* **2022**, *61* (46), No. e202212816, DOI: 10.1002/anie.202212816.
(32) Zhang, Y.; Wang, Y.; Xia, H.; Gao, P.; Cao, Y.; Jin, H.; Li, Y. A Hybrid ZIF-8/ZIF-62 Glass Membrane for Gas Separation. *Chem. Commun.* **2022**, *58* (68), 9548−9551.
(33) Wang, Y.; Jin, H.; Ma, Q.; Mo, K.; Mao, H.; Feldhoff, A.; Cao, X.; Li, Y.; Pan, F.; Jiang, Z. A MOF Glass Membrane for Gas Separation. *Angew. Chem., Int. Ed.* **2020**, *59* (11), 4365−4369, DOI: 10.1002/anie.201915807.
(34) Lee, S.; Cho, I.-S.; Lee, J. H.; Kim, D. H.; Kim, D. W.; Kim, J. Y.; Shin, H.; Lee, J.-K.; Jung, H. S.; Park, N.-G.; Kim, K.; Ko, M. J.; Hong, K. S. Two-Step Sol−Gel Method-Based TiO_2 Nanoparticles with Uniform Morphology and Size for Efficient Photo-Energy Conversion Devices. *Chem. Mater.* **2010**, *22* (6), 1958−1965.
(35) Wang, C.-C.; Ying, J. Y. Sol−Gel Synthesis and Hydrothermal Processing of Anatase and Rutile Titania Nanocrystals. *Chem. Mater.* **1999**, *11* (11), 3113−3120.
(36) *Basic Principles of Membrane Technology*; Kluwer Academic Publishers: Dordrecht, 1996; pp 224−225.
(37) Zhu, J.; Li, P.-Z.; Guo, W.; Zhao, Y.; Zou, R. Titanium-Based Metal-Organic Frameworks for Photocatalytic Applications. *Coord. Chem. Rev.* **2018**, *359*, 80−101.
(38) Hayashi, K.; Takahashi, M.; Nomiya, K. Novel Ti−O−Ti bonding species constructed in a metal-oxide cluster. *Dalton Trans.* **2005**, *23*, 3751−3756.
(39) Wang, Y.; Sun, T.; Yang, D.; Liu, H.; Zhang, H.; Yao, X.; Zhao, H. Structure, reactivity, photoactivity and stability of Ti−O based materials: a theoretical comparison. *Phys. Chem. Chem. Phys.* **2012**, *14* (7), 2333−2338.

https://doi.org/10.1021/acsami.4c00857
ACS Appl. Mater. Interfaces 2024, 16, 17016−17024